Accepted Manuscript

Liver vessel segmentation and identification based on oriented flux symmetry and graph cuts

Ye-zhan Zeng , Yu-qian Zhao , Ping Tang , Miao Liao ,
Yi-xiong Liang , Sheng-hui Liao , Bei-ji Zou

Please cite this article as: Ye-zhan Zeng , Yu-qian Zhao , Ping Tang , Miao Liao , Yi-xiong Liang , Sheng-hui Liao , Bei-ji Zou , Liver vessel segmentation and identification based on oriented flux symmetry and graph cuts, *Computer Methods and Programs in Biomedicine* (2017), doi: 10.1016/j.cmpb.2017.07.002

Highlights

- The combination of optimal oriented flux and oriented flux antisymmetry measures is used to yield slenderized vessels
- A thin-vessel centerline extraction method is proposed based on height ridge traversal and leaf node line-growing
- Our method can effectively extract thin vessels
- Our method can identify hepatic vein and portal vein

Liver vessel segmentation and identification based on oriented flux symmetry and graph cuts

Ye-zhan Zeng [a, b], Yu-qian Zhao [a, b *], Ping Tang [a, b], Miao Liao [c], Yi-xiong Liang [a], Sheng-hui Liao [a], Bei-ji Zou [a]

[a] *School of Information Science and Engineering, Central South University, Changsha 410083, China*
[b] *Department of Biomedical Engineering, Central South University, Changsha 410083, China*
[c] *School of Computer Science and Engineering, Hunan University of Science and Technology, Xiangtan 411201, China*

* Contact: zyq@csu.edu.cn

Abstract: ***Background and Objective***: Accurate segmentation of liver vessels from abdominal computer tomography angiography (CTA) volume is very important for liver-vessel analysis and living-related liver transplants. This paper presents a novel liver-vessel segmentation and identification method. ***Methods***: Firstly, an anisotropic diffusion filter is used to smooth noise while preserving vessel boundaries. Then, based on the gradient symmetry and antisymmetry pattern of vessel structures, optimal oriented flux (OOF) and oriented flux antisymmetry (OFA) measures are respectively applied to detect liver vessels and their boundaries, and further to slenderize vessels. Next, according to vessel geometrical structure, a centerline extraction measure based on height ridge traversal and leaf node line-growing (LNLG) is proposed for the extraction of liver-vessel centerlines, and an intensity model based on fast marching is integrated into graph cuts (GCs) for effective segmentation of liver vessels. Finally, a distance voting mechanism is applied to separate the hepatic vein and portal vein. ***Results***: The experiment results on abdominal CTA images show that the proposed method can effectively segment liver vessels, achieving an average accuracy, sensitivity, and specificity of 97.7%, 79.8%, and 98.6%, respectively, and has a good performance on thin-vessel extraction. ***Conclusions***: The proposed method does not require manual selection of the centerlines and vessel seeds, and can effectively segment liver vessels and identify hepatic vein and portal vein.

Key words: Liver vessel segmentation; Optimal oriented flux (OOF); Oriented flux antisymmetry (OFA); Height ridge traversal; Leaf node line-growing (LNLG); Graph cuts

1. Introduction

In medical practice, an analysis of liver-vessel structures is usually a prior step for liver disease diagnosis and surgery planning [1]. For example, surgery doctors depend on liver-vessel morphology and branching pattern to choose optimal operation scheme. However, due to inhomogeneous background, serious noise and low contrast as well as various geometrical structures from patient to patient, an accurate segmentation of liver vessels is a challenging task. In practice, to obtain accurate segmentation results, the radiologists need to manually delineate vessel contours slice by slice, which is very tedious and time-consuming, and highly relies on experience and skills of radiologists. Therefore, automatic or semi-automatic liver-vessel segmentation is necessary and has attracted increasing attention.

Many works have been made to detect/enhance 3D vessels [2]. Generally, the vessels in medical images can be considered as tubular structures with radially symmetric cross-sections. Based on this intuitional shape characteristic, some Hessian-based measures are frequently employed for vessel detection. Frangi et al. [3] proposed an ellipsoid model according to Hessian-based features for the detection of tubular-like structures. Following Frangi's model, Jerman et al. [4] proposed a 3D vessel filter based on the ratio of Hessian eigenvalues to obtain a better close-to-uniform response in vessel nodules and bifurcations. A medialness filter was presented by Krissian et al. [5] to detect vessel geometrical structures depending on Hessian to find the tangent direction and boundary gradient to estimate corresponding radii. Considering Hessian matrix as a stress tensor, Xiao et al. [6] developed a strain energy filter to handle local deformations like vessel junctions.

For the segmentation of 3D vessels, Yan and Kassim [7] introduced a capillary force to guide the evolution of surface into thin vessels. Motivated by the motion of solid surface under a liquid pressure, Law and Chung [8] proposed a deformable surface model for intracranial and cardiac vessel segmentation. Cheng et al. [9] described an active contour framework with shape and size constrains on the cross-section of vessels. It begins with a vessel axis tracking in a 3D CT data, followed by vessel boundary delineation on the vessel cross-section from this axis, and then applies an active contour model to segment vessels under constrained movements. In [10], Esneault et al. applied a 3D geometrical moment-based detector and graph cuts(GCs) for liver-vessel segmentation, and the experiments on CT dataset prove it is robust against the noisy data and can overcome sharking bias on elongated vessel structures.

Recently, Law et al. [11] presented a method based on intensity discontinuity-homogeneity (DH) ratio for intracranial vessel segmentation. Their method was verified on the phase contrast magnetic resonance angiographic (PC-MRA) images, and indicated a good performance to deal with the intensity varying vasculatures. Based on the vessel properties like intensity and direction, Chi et al. [12] presented a liver-vasculature segmentation method, which first locally groups voxels into vessel branches by a junction measurement, and then globally groups voxels into different vessel systems using a multiple feature point voting mechanism. Schneider et al. [13] introduced two vessel filters including orthogonal subspace and steerable filters to extract vessel features, and devised a machine learning-based framework for 3D vessel segmentation and centerline extraction by oblique random forests and Hough voting. Zeng et al. [14] reported a fully

automated method for the segmentation of liver vessels using the combination of four vessel filters and an Extreme Learning Machine (ELM). Hemmati et al. [15] developed a 3D level set method for carotid-lumen segmentation, which starts with a mean shift filter to improve the uniformity of vessels, followed by a fast marching algorithm to extract the centerlines and then uses a 3D level set to conduct segmentation.

Owing to the complexity of 3D liver-vessel images, especially for the existence of some weak and variable thin vessels, few investigations have been reported for 3D liver-vessel segmentation. In this paper, we propose a liver-vessel segmentation and identification approach based on the combination of oriented flux symmetry and GCs. At first, liver images are smoothed by an anisotropic diffusion filter to remove noise while preserving vessel boundaries. Then, OOF and OFA measures are used to detect liver vessels and their corresponding boundaries, and further to slenderize vessels. Next, liver-vessel centerlines are extracted from the slenderized vessel images, followed by a fast marching method on the OOF detection result to roughly segment vessels. Finally, GCs combined with intensity model is used for vessel refinement, and a distance voting mechanism is applied to identify the hepatic vein and portal vein. The propose method requires neither manual interaction for object region selection nor sophisticated training procedure, and is capable of dealing with complex liver-vessel systems. A main flowchart of the proposed method is shown in Fig. 1.
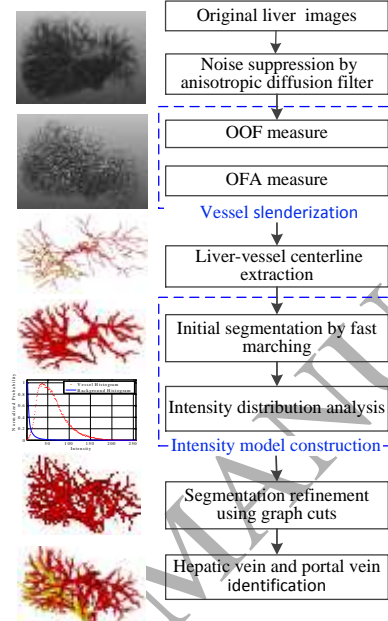

Fig. 1. Flowchart of the proposed method.

2. Methodology

2.1. Preprocessing

Due to the similar geometrical structure or intensities, liver-vessel segmentation is sensitive to some irrelevant organs or tissues, such as ribs and kidneys. In addition, it is a significant computational burden to segment liver vessels from the whole abdominal dataset, and therefore, liver-vessel segmentation is conducted only in the registered liver region obtained in our previous studies [16, 17]. To give an intuitive illustration, Fig. 2 displays an example for the generation of 3D liver image. As liver vessels in these images suffer from serious noise, a nonlinear anisotropic diffusion filter proposed by Perona and Malik [18] is used to filter noise as well as keep the vessel boundaries:

$$\begin{cases} \dfrac{\partial I(x,t)}{\partial t} = div(c(|\nabla I|) \cdot \nabla I) \\ I(x,0) = I_0(x) \end{cases} \tag{1}$$

where $I(x,t)$ is the gray level of voxel x at time t, $I_0(x)$ is the original 3D liver image, and div and ∇ represent the divergence and gradient operators, respectively. The conduction coefficient $c(|\nabla I|)$ denotes a monotonically decreasing function as the image gradient increases, and is defined as:

$$c(|\nabla I|) = e^{-(\|\nabla I\|/d)^2} \tag{2}$$

where d is a threshold controlling the diffusion rate, and is set as 70 in this paper. The anisotropic diffusion filter is implemented by Insight Segmentation and Registration Toolkit (ITK), an open-source software widely used for medical image processing (http://www.itk.org), and its iteration number is empirically set as 3.
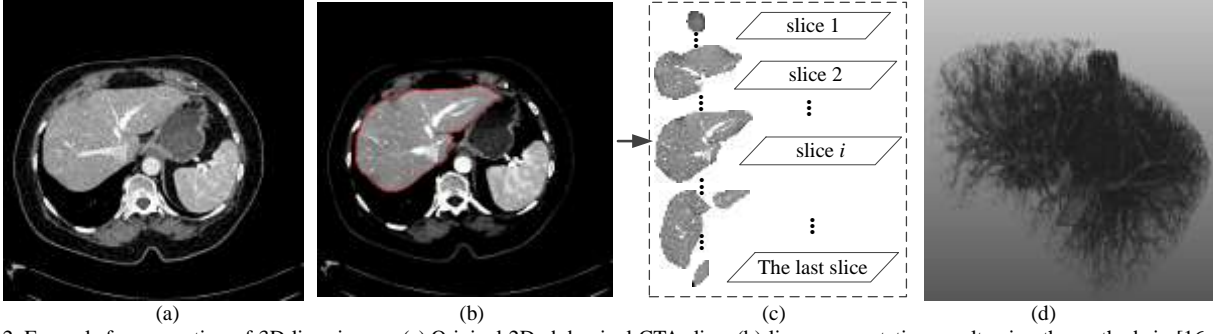
Fig. 2. Example for generation of 3D liver image. (a) Original 2D abdominal CTA slice, (b) liver segmentation result using the methods in [16, 17], where the region surrounded by a red contour is the segmented liver, (c) procedure of 3D liver generation, and (d) 3D liver image visualization, which is implemented in MeVisLab modular framework, a powerful framework for medical image visualization as described in [19].

2.2. Vessel slenderization

Vessel slenderization is used to highlight liver-vessel centers which can help to extract liver-vessel centerlines. It is performed by a combination of OOF and OFA measures based on the analysis of oriented flux symmetry for the vessel centers and boundaries [20, 21].

2.2.1. Oriented Flux Symmetry

Many existing vessel filters depend on scaled Hessian matrix to detect tubular structures, and the Hessian matrix is obtained by convolving the image with second order derivative of Gaussian smoothing function. As is well known, Gaussian smoothing may lead to the blurring of object boundaries. To partly overcome this issue, two measures including OOF and OFA are applied based on the quantification of image gradient symmetry in vessel centers and antisymmetry in vessel boundaries [21, 22]. These two measures are also referred to as oriented flux symmetry.

The OOF measure is based on the oriented flux theory, whose purpose is to quantify the gradient symmetry. Briefly, the oriented flux measure aims at computing the amount of image gradient projection taken in a direction $\hat{\rho}$ around a local sphere surface, and can be defined as

$$f\left(x;r,\hat{\rho}\right)=\frac{1}{4\pi r^2}\int_{\partial B_r}\left(\left(\nabla\left(G_{\sigma_0}*I\right)\left(x+A\right)\cdot\hat{\rho}\right)\hat{\rho}\right)\cdot\hat{\mathbf{n}}dA \tag{3}$$

where B_r is a local spherical region with a radius r and its center x, G_{σ_0} the Gaussian with a small standard deviation σ_0 typically equal to voxel spacing, A the position vector on ∂B_r, $\hat{\mathbf{n}}$ the inward normal of the sphere at A, and dA represents the infinitesimal area on ∂B_r. Due to the high sensitivity to symmetric gradient pattern, $f\left(x;r,\hat{\rho}\right)$ reaches its maximum when r is equal to the structure radius and $\hat{\rho}$ is along the tubular structure, and $f\left(x;r,\hat{\rho}\right)$ decreases where position x is away from the structure center.

To investigate the antisymmetric gradient pattern, the OFA measure is defined as

$$s(x;r,\hat{\rho})=\frac{1}{4\pi r^2}\int_{\partial B_r}\left(\nabla\left(G_{\sigma_0}*I\right)\left(x+A\right)\cdot\hat{\rho}\right)dA \tag{4}$$

which is used to quantify the antisymmetry of the image gradient. It is sensitive to and takes high value for antisymmetrical gradient patterns such as object boundaries, and vanishes for symmetric gradient patterns.

2.2.2. Gradient Symmetry Quantification with OOF and OFA

The quantified gradient symmetry aims at slenderizing vessels by combining the OOF and OFA, and performs eigenvalue decomposition on a tensor to obtain the optimal projection direction maximizing the magnitude of f. For a 3D image, f can be rewritten as a quadratic form of $\hat{\rho}^T\mathbf{Q}_{x,r}\hat{\rho}$, where $\mathbf{Q}_{x,r}$ is a 3×3 oriented flux matrix [18] whose entry at the ith row and j^{th} column ($i,j\in\{1,2,3\}$) is given by

$$q_{x,r}^{i,j}=\frac{1}{4\pi r^2}\left(\partial_{i,j}G_{\sigma_0}(x)*b_{r,x}(y)*I(x)\right) \tag{5}$$

where y is a position coordinate, and $b_{r,x}$ is a step function defined as

$$b_{r,x}(y)=\begin{cases}1, & \|y-x\|\le r,\\0, & \text{otherwise.}\end{cases} \tag{6}$$

Assuming λ_1, λ_2, and λ_3 are the eigenvalues of $\mathbf{Q}_{x,r}$, and are sorted in order, e.g. $|\lambda_1|\ge|\lambda_2|\ge|\lambda_3|$, a bright vessel

structure will have $\lambda_1 \approx \lambda_2 < 0$ with their corresponding eigenvectors $\mathbf{e}_1$ and $\mathbf{e}_2$ defining the cross-section plane, while $\mathbf{e}_3$ denoting the vessel tangent direction. According to oriented flux theory, the OOF can be denoted as the amount of the image gradient pointing to the structure center along two orthogonal directions $\mathbf{e}_1$ and $\mathbf{e}_2$, and can be defined as

$$f_{OOF}(x,r) = \frac{1}{4\pi r^2} \int_{\partial B_r} \left([\mathbf{e}_1(x;r) \ \mathbf{e}_2(x;r)]^T \nabla (G_{\sigma_0} * I)(x+A) \right) \cdot \left([\mathbf{e}_1(x;r) \ \mathbf{e}_2(x;r)]^T \hat{\mathbf{n}} \right) dA \quad (7)$$
$$= f(x;r,\mathbf{e}_1(x,r)) + f(x;r,\mathbf{e}_2(x,r)) = \lambda_1(x,r) + \lambda_2(x,r)$$

Utilizing Eq. (4), an OFA based measure combined with $\mathbf{e}_1$ and $\mathbf{e}_2$ is allowed to investigate the antisymmetry of gradients along the structure cross-sectional plane, and can be defined as

$$f_{OFA}(x,r) = \frac{1}{4\pi r^2} \left| \int_{\partial B_r} \left([\mathbf{e}_1(x;r) \ \mathbf{e}_2(x;r)] \right)^T \nabla (G_{\sigma_0} * I)(x+A) dA \right| \quad (8)$$
$$= \sqrt{s^2(x,r,\mathbf{e}_1) + s^2(x,r,\mathbf{e}_2)}$$

Based on the intensity distribution of f_{OOF} and f_{OFA}, a measure for generating significant response in the middle of the structure is defined as $\max(0, f_{OOF}(x,r) - f_{OFA}(x,r))$. In addition, a traditional multi-scale framework over different radii is adopted to obtain the maximal response, and is defined as

$$M(x) = \max_{r \in R} \left(\max(0, f_{OOF}(x,r) - f_{OFA}(x,r)) \right) \quad (9)$$

where R is a set of radius specified as $R = \{1, 2, 3, ..., 7\}$ voxels, and

$$f_{OOF}(x) = \max_{r \in R} (f_{OOF}(x,r)) \quad (10)$$
$$f_{OFA}(x) = \max_{r \in R} (f_{OFA}(x,r)) \quad (11)$$

The scale maximizing the response of Eq. (9) is further applied to estimate the vessel radius $r' = \arg\max_{r \in R} (M(x))$ and the corresponding tangent direction $\mathbf{t} = \mathbf{e}_3$, which will be utilized for the extraction of vessel centerlines.

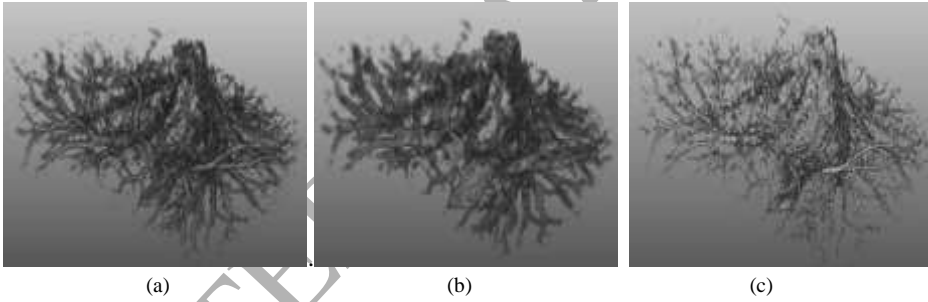Fig. 3. Vessel detection results from Fig. 2(d). Responses of (a) OOF, (b) OFA, and (c) $M(\cdot)$.

Figures 3(a)-(c) show the vessel detection results of f_{OOF}, f_{OFA}, and $M(\cdot)$, respectively. Compared with Figs. 3(a) and (b), the intensities of Fig. 3(c) at the vessel centers keep higher values while drop sharply at the vessel boundaries, based on which, the vessels generated by Eq. (9) are named as the slenderized vessels in this paper, and the following vessel-centerline extraction is conducted on these slenderized vessels.

2.3. *Vessel-centerline extraction*

The purpose of vessel-centerline extraction is to provide seed points for initial vessel segmentation and identify different vessel systems. Usually, the traditional vessel-centerline extraction methods heuristically track the centerlines in enhanced vessel images from the given seed points. The drawbacks of these methods include: 1) they need manually selected seed points, which is time-consuming and boring due to the complexity of liver vessels in CTA images; 2) it is difficult to separate centerlines belonging to different systems as well as effectively extract thin-vessel centerlines. To solve these problems, a novel vessel-centerline extraction method based on height ridge traversal and leaf node line-growing (LNLG) is proposed.

As discussed in Section 2.2.2, the intensities of $M(\cdot)$ in vessel centers are obviously higher than those on vessel boundaries, i.e., the higher the intensities, the more likely these voxels belong to the vessel centerlines. Therefore, the height ridge traversal method, which tracks the centerlines along neighboring voxels of the highest intensity, is used to extract centerlines from the slenderized vessel image $M(\cdot)$ rather than from the traditional enhanced image like Frangi filtering response.
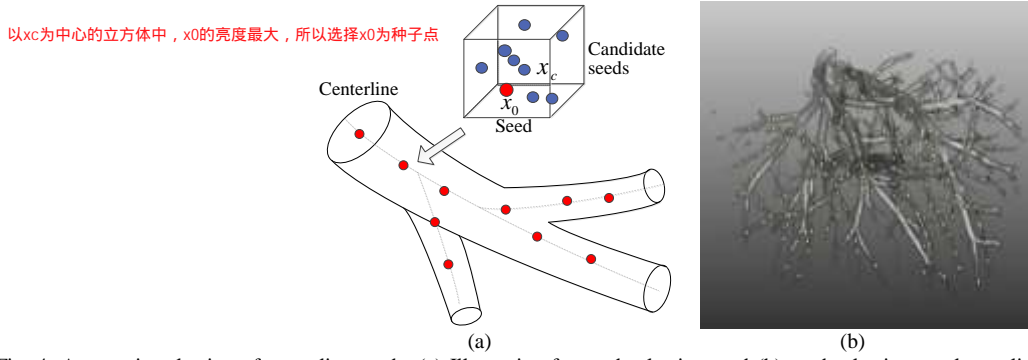
Fig. 4. Automatic selection of centerline seeds. (a) Illustration for seed selection, and (b) seed selection results on liver vessels. The blue and red points in (a) represent the candidate seeds (x_c s) and final selected seeds (x_0 s), respectively. Note that as one voxel is difficult to be highlighted in 3D image, each seed in (b) is represented by eight voxels and is marked in yellow for better vision. In addition, due to the visual limitation, some seeds whose neighboring voxels appear with high intensity (indicated by white color in (b)) fail to be visualized, but can be extracted in our experiments.

Instead of manual selection of seed points, we first choose the voxels in $M(\cdot)$ whose intensities are above a threshold th_{seed} as candidate seeds x_c s as shown by the blue points in Fig. 4(a), and then construct a cubic region centered at each x_c and set the voxel with highest intensity inside each cubic region as the final selected seeds x_0 s, as shown by the red points in Fig. 4(a). Due to the significant difference between the vessel center and boundary in $M(\cdot)$, this procedure can extract almost all centerline seeds, except for a possible slight deviation from x_0 to the ideal vessel center for few centerline seeds. Figure 4(b) shows a final result for automatic selection of centerline seeds (marked in yellow) on liver vessels, from which we can observe that the centerline seeds can be efficiently selected in spite of low contrast.

Next, a height ridge traversal algorithm is applied to extract vessel centerlines, which starts from the selected seed x_0 and tracks the height ridge towards both its positive and negative tangent directions $\mathbf{t}_0$ and $-\mathbf{t}_0$. For each current centerline voxel x_i with tangent direction $\mathbf{t}_i$, its all local neighbors x_i^n satisfying $\overrightarrow{x_i x_i^n} \cdot \mathbf{t}_i > 0$ and $M(x_i^n) > th_{low}$, where th_{low} is a given threshold, are treated as candidate centerline voxels, and among them the neighbor with the highest value of $M(\cdot)$ is selected as the next centerline voxel x_{i+1}. To keep the traversal direction, the tangent direction $\mathbf{t}_{i+1}$ is set as $\mathbf{t}_{i+1} = \mathrm{sign}\left(\overrightarrow{x_i x_{i+1}} \cdot \mathbf{t}_{i+1}\right)\mathbf{t}_{i+1}$. This procedure is performed iteratively along the height ridge until no voxels satisfy the above conditions; however, some isolated centerlines may be generated due to low intensity and serious noise. For some short isolated centerlines, say less than 10 voxels, they can be directly removed, while for longer ones, they will be linked according to geometrical constraints [23]. For example, the corresponding vessel radius of the endpoint voxel on the isolated centerline should be smaller than that of the voxel on the centerline to be linked, and the connection distance must not be too large (e.g. 8 voxels). Finally, each vessel centerline is assigned to a corresponding label for the identification of hepatic vein and portal vein, as shown in Fig. 5(b), whose original slenderized vessel image is shown in Fig. 5(a). To vividly display different vessel centerlines, the visualization of the color images in Fig. 5 is implemented using publicly available Visualization Toolkit (VTK) software (http://www.vtk.org).
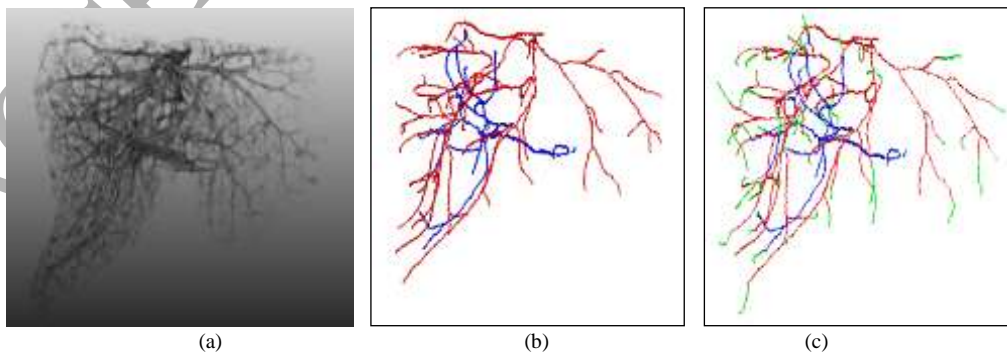

Fig. 5. Example of vessel-centerline extraction. (a) Slenderized vessel image, (b) vessel centerlines extracted by height ridge traversal, and (c) vessel centerlines extracted by the combination of the height ridge traversal with LNLG, where the red and blue lines respresent the centerlines of hepatic vein and potral vein, respectively, and the green lines are the results of LNLG.

During the vessel-centerline extraction, th_{low} is a key parameter. For example, a lower th_{low} helps to extract more centerline voxels for thin vessels, and at the same time easily leads to two parallel or intertwined vessel centerlines of different vessel systems being mistaken as one vessel centerline. On the contrary, a larger th_{low} is more beneficial to

identify different vessel systems, while will result in the loss of thin-vessel centerlines. To effectively extract thin-vessel centerlines as well as identify different vessel systems, a leaf node line growing (LNLG) measure is developed and applied on the extracted vessel centerlines, which further seeks the centerline voxels of thin vessels with a lower threshold th_{leaf} ($th_{leaf} < th_{low}$) starting from centerline endpoint voxels (as the liver-vessel centerlines are similar to topological tree structures, as shown in Fig. 5(b), the centerline endpoint voxels are named as leaf nodes for visual description), and assigns these centerline voxels the same label as their corresponding leaf node. Its main steps include:

Step 1. Leaf node location

The leaf node of vessel centerline is usually located by calculating the number of its neighboring voxels. For example, the voxel with one neighbor is considered as a leaf node. However, some leaf nodes might include more than one neighbor like 'L' and 'T' shapes. Therefore, besides the number of neighboring voxels, the tangent direction of voxel also needs to be considered.

For a centerline voxel x_i, its neighboring voxels on the vessel centerline can be classified into two groups according to their directions of position vectors $\overrightarrow{x_i x_i^n}$ following or against the tangent direction. To describe this property, a signed position vector is introduced based on the tangent direction $\rho_i = \overrightarrow{x_i x_i^n} \cdot \mathbf{t}_i$. If $\rho_i > 0$, the direction of position vector $\overrightarrow{x_i x_i^n}$ follows the tangent direction, otherwise is against the tangent direction. As a leaf node, its neighboring voxels on the vessel centerline only belong to either of the two groups. Therefore, we can utilize the following condition to determine whether the voxel x_i is a leaf node or not:

$$x_i \begin{cases} \text{a leaf node,} & \text{if all } x_i^n \text{ s.t. } \rho_i > 0, \text{ or all } x_i^n \text{ s.t. } \rho_i \le 0 \\ \text{not a leaf node,} & \text{else.} \end{cases} \tag{12}$$

Step 2. Line-growing

The line-growing is used to extract the centerlines of thin vessels starting from the leaf node denoted by x_e, the direction of which is obtained by the analysis of ρ_e and tangent direction $\mathbf{t}_e$. Intuitively, the direction of line-growing is along centerline and towards the thin vessels, i.e., it should be opposite to the direction of position vector $\overrightarrow{x_e x_e^n}$, where x_e^n is the neighboring voxel x_e on the vessel centerline. As introduced in step 1, $\rho_e > 0$ indicates $\overrightarrow{x_e x_e^n}$ follows $\mathbf{t}_e$, and therefore, the line-growing direction $\mathbf{t}_{line}$ should be opposite to $\mathbf{t}_e$, otherwise the same direction as $\mathbf{t}_e$. According to the discussion above, $\mathbf{t}_{line}$ can be expressed as

$$\mathbf{t}_{line} = -\text{sign}(\rho_e) \cdot \mathbf{t}_e \tag{13}$$

Similarly to the extraction of vessel centerline introduced early, we choose the leaf node as the seed point and apply the height ridge traversal algorithm to further extract the centerline of thin vessels along the direction $\mathbf{t}_{line}$ with threshold th_{leaf}, as shown by the green lines in Fig. 5(c), from which we can observe that this method can efficiently extract vessel centerlines, especially for thin vessels with low contrast.

2.4. Liver-vessel segmentation

The proposed method for liver-vessel segmentation mainly includes initial segmentation by a fast marching technique [24] and vessel refinement by GCs. Usually, the GCs based methods need initial object regions to obtain their intensity distribution [25, 26]. To avoid manual selection of object regions, a fast marching technique is firstly applied on the OOF detection result to segment vessels initially, in which the voxels on the centerline are chosen as the seeds. Then, based on the initial segmented vessels, an intensity model is proposed by estimating different gray level probabilities on vessels and background, which can be expressed by

$$\begin{cases} h_{obj}(r_k) = n_{o_k} / n_o \\ h_{bkg}(r_k) = n_{b_k} / n_b \end{cases} \tag{14}$$

where r_k, $k = 0, 1, 2, ..., 255$, represents the kth gray level, n_{o_k} and n_{b_k} are the voxel numbers of vessel and background regions, respectively, in OOF detection result with their gray level r_k, and n_o and n_b represent the maximal numbers of o_k and b_k, respectively, for all gray levels. Figure 6 displays an example of intensity model, where the red dot line and blue solid line represent h_{obj} and h_{bkg}, respectively.
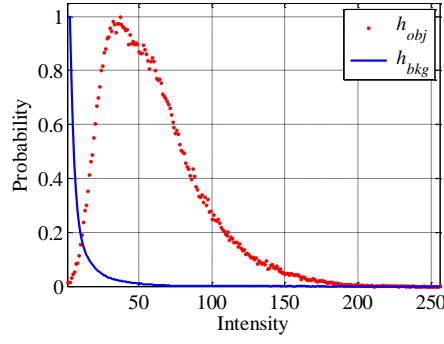
Fig. 6. Example of intensity model. The red dot line and blue solid line represent h_{obj} and h_{bkg}, respectively.

In this paper, the intensity model is integrated into the GCs for liver-vessel segmentation, and the energy function can be constructed as

$$E = \mu \sum_{p \in P} R_p(L_p) + \sum_{\{p,q\} \in N, L_p \neq L_q} B_{pq}(L_p, L_q) \qquad (15)$$

where R and B represent the region term and boundary term, respectively, N is the set of neighboring voxels, L is a mapping function from set of voxels P to the set of binary labels, and μ is the weight coefficient set as 1. The region term R_p is used to measure the cost of voxel p to object and background, and the boundary term is used to penalize the discontinuity between voxel pairs p and q.

Typically, the region term R_p is expressed by a negative log-likelihood by assigning the voxel p to object and background, and is usually obtained by analyzing their intensity distributions. As observed from Fig. 6, the intensities of vessels mainly lie in a range of [20, 100], while those of background obviously approximate to 0. Therefore, intensity model is helpful to differentiate vessels from background. Taking this into account, we define the region term as:

$$\begin{cases} R_p(obj) = -\ln(h_{obj}(f_{oof}(p))) \\ R_p(bkg) = -\ln(h_{bkj}(f_{oof}(p))) \end{cases} \qquad (16)$$

where obj and bkg represent foreground and background, respectively.

As presented in Section 2.3, the OFA measure can effectively capture the boundaries of tubular structures like vessels, and the boundary term is therefore given by

$$B_{pq} = \exp\left(-\frac{(f_{OFA}(p) - f_{OFA}(q))^2}{2}\right) \cdot \frac{1}{dist(p,q)} \qquad (17)$$

where $dist(p,q)$ is the distance between voxels p and q.

2.5. Liver vessel identification

Due to similar intensity distribution and blurry boundaries, the intertwined and parallel vessel branches segmented by GCs may be incorrectly grouped into the same ones. To identify different vessels, a distance voting mechanism is developed based on the vessel geometrical structure.

Intuitively, the shorter the Euclidean distance from a vessel voxel to the centerline of a hepatic/portal vein, the more likely the voxel belongs to the hepatic/portal vein. Based on this consideration, the minimum Euclidean distances from each vessel voxel to the centerline of hepatic vein and portal vein are calculated, respectively, and are denoted by d_h and d_p. Then, we apply the distance voting mechanism to separate hepatic vein from portal vein, which can be defined as:

$$v \subset \begin{cases} \text{hepatic vein,} & \text{if } d_h < d_p \\ \text{portal vein,} & \text{else.} \end{cases} \qquad (18)$$

where v is the liver-vessel segmentation result.

3. Experiments and results

The experiments are conducted based on our previous works [14, 16, 17], which are tested on clinical CTA volumes at portal venous phase. Each slice has an axis plane resolution of 512×512 pixels with thickness of 0.5-2 mm. The window width /level of CTA volumes is set in a range of [400, 600]/[300, 500] Hounsfield Units (Hu) depending on different CTA images. The slenderized vessel image is normalized to [0, 255], the thresholds th_{seed} and th_{leaf} for

vessel-centerline extraction are respectively set as 40 and 20, and the parameter th_{low} is empirically set in a range of [25, 30]. All experiments are carried out on a personal computer configured with an i7-2600 3.4 GHz CPU, 16 GB RAM memory, AMD Radeon R9 280x GPU, and a 64-bit Windows 7 Operating System.

Due to the lack of a publicly available database, the proposed method is only conducted on six self-created clinical CTA data sets, and the segmentation results of the proposed method are compared with those of the classical geodesic active contour (GAC) [27], active contour without edge (also called CV model) [28], and the methods in [29] and [14] (For further details of the above four methods, please refer to our previous work [14]). To receive the best possible results, the centerline voxels are naturally set as the object regions for GAC and CV model, and all the methods are implemented only in the liver region to reduce the disturbance of irrelative tissues or organs such as ribs and spleen. In addition, their parameters are optimized depending on specific CTA volumes.
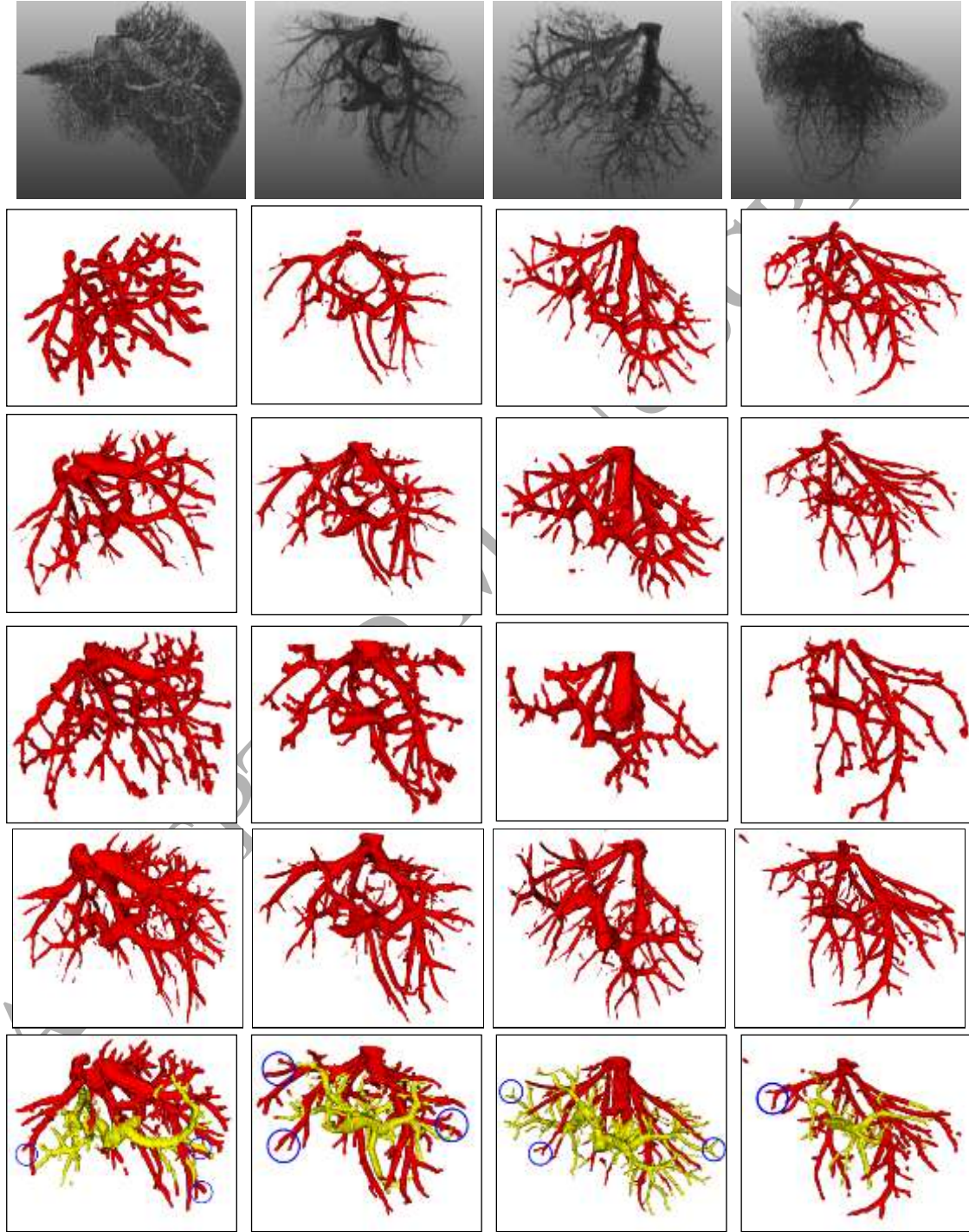

Fig. 7. Liver-vessel segmentation results of different methods. The first row shows four liver-vessel images, and the subsequent five rows denote their corresponding liver-vessel segmentation results by GAC, CV model, the methods in [29] and [14], and the proposed method, respectively. Note that the red and yellow regions in the last row represent the hepatic vein and portal vein, respectively.

Figure 7 gives four segmentation results of liver vessels with different geometrical structures, in which the first row shows original liver-vessel images, and the subsequent five rows represent their corresponding segmentation results of

GAC, CV model, the method in [29], our previous approach [14], and the proposed method, respectively. As observed, compared with the GAC, CV model, and the methods in [29] and [14], the proposed method can detect more thin vessels, as shown in the closed blue circles in the last row of Fig. 7. In addition, it also can distinguish hepatic vein and portal vein, as labeled by the yellow and red regions in the last row of Fig. 7, and the ratio of the number of voxels correctly identified as hepatic and portal veins to that of all the vessel voxels extracted by GCs is up to 89.2%. The detailed descriptions of hepatic vein and portal vein can be referred to the study in [30].

To evaluate the segmentation performance quality, a radiologist with rich experience is invited to establish the ground truth of liver vessels. The evaluation task is firstly implemented by a trained operator to acquire initial liver-vessel segmentation results using ITK-SNAP tool, which allows users to manually delineate anatomical regions of interest. With the aid of the radiologist, these segmentation results are subsequently corrected slice by slice. For quantitative analysis, we use three measures described in [31] and [32] including accuracy, sensitivity, and specificity, to assess the segmentation performance:

$$Accuracy = \frac{TP + TN}{TP + FN + TN + FP} \qquad (19)$$

$$Sensitivity = \frac{TP}{FP + TN} \qquad (20)$$

$$Specificity = \frac{TN}{FP + TN} \qquad (21)$$

where TP and TN represent the number of voxels correctly classified as vessel and background voxels, respectively, and FP and FN indicate the number of voxels wrongly classified as the vessel and background voxels, respectively.

Table 1 Segmentation performances of different methods

Methods	Accuracy	Sensitivity	Specificity
GAC	0.966	0.357	0.996
CV model	0.977	0.713	0.990
Method in [14]	0.981	0.742	0.993
Method in [29]	0.970	0.571	0.990
Ours	0.977	0.798	0.986

Table 1 illustrates the segmentation performances of different methods, from which we can see that the average segmentation accuracy, sensitivity, and specificity of the proposed method are up to 97.7%, 79.8%, and 98.6%, respectively, and the average accuracy and specificity are approximate to those of GAC, CV model and the methods in [29] and [14], while the sensitivity is obviously higher than that of the other four methods.

The segmentation performance can also be evaluated by analyzing the error distances from the incorrectly segmented voxels to the nearest vessel boundary of ground truth. Figure 8 shows a histogram of the error distances for different methods, from which we can see that the error distances of the proposed method mostly range in a voxel length, and the number of incorrectly segmented voxels is smaller than that of GAC, CV model and the methods in [29] and [14].
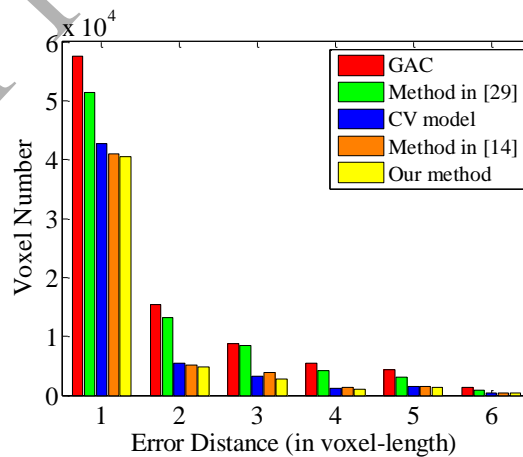

Fig. 8. Histogram of error distances from the incorrectly segmented voxels to the nearest vessel boundary in the ground truth for different methods.

4. Discussion

In this study, we propose an oriented flux symmetry and GCs method for liver-vessel segmentation and identification. The main challenge of liver-vessel segmentation comes from the presence of the low contrast and intensity inhomogeneity in CTA images, which often leads to a poor segmentation and incorrect identification. To tackle this problem, the combination of OOF and OFA measures is used to yield a slenderized vessel image and for the first time, a

novel centerline extraction method is proposed and applied on this slenderized vessel image, which has been shown to be effective in the extraction of thin-vessel centerlines, and also in the identification of different vessel centerlines. The proposed method receives a good performance with empirically set parameters th_{seed}, th_{leaf}, and th_{low}. The intensity distribution of liver vessels provides a metric to separate vessels from liver parenchyma, and thus an intensity model based on fast marching is presented to estimate the liver intensity features.

Since the intensity model and boundary information obtained by OFA measure are learnt from each specific CTA volume, the proposed method can deal with the variations on the geometrical structures of different vessels, as shown in Fig. 7, and the its results contain more thin vessels compared with some existing segmentation methods. For example, the GAC method is usually applied for thin-vessel segmentation with a larger propagating coefficient, which easily causes to the evolution curve/surface to expand beyond the weak vessel boundaries and therefore results in a serious over-segmentation. Due to the similar intensity between thin vessels and background region, the region growing algorithm is difficult to segment thin vessels.

Influenced by the similar intensity and partial volume effects, the hepatic vein is quite hard to be differentiated from the portal vein, which may lead to the fact that many intertwined and parallel vessels belonging to different vessel systems are mistakenly classified into the one vessel system, and few methods in the literatures are reported to solve this problem. In this paper, based on the analysis of the shortest distances from vessel voxels to two different vessel centerlines, an efficient distance voting mechanism is adopted for identification of hepatic vein and port vein.

Experiments on the abdominal CTA volumes show that the proposed method achieves average accuracy, sensitivity, and specificity of 97.7%, 79.8%, and 98.6%, respectively, and the error distances from the incorrectly segmented voxels to the closest vessel boundary of ground truth are mostly in a one-voxel length. The ratio of the number of the correctly identified voxels to that of the whole vessel voxels is also up to 89.2%. This is mainly because more centerlines of thin vessels can be extracted by the height ridge traversal and LNLG proposed in our method, which therefore help to establish an effective intensity model for vessel refinement in GCs.

Presently, our method mainly focuses on effective extraction of vessel centerlines as well as the identification of different vessel systems, and there are also some weaknesses. For example, it achieves good performance only on high contrast CTA images, which is a common problem for the intensity- and gradient- based methods like region growing and GAC, and it can be improved by introducing an extra estimated tubular likelihood into the energy function of GCs like the method in [10]. In addition, although the implementation of multi-scale OOF and OFA has been optimized by Fast Fourier Transform, the running time is still up to 6.5 minutes in our current CPU-based platform for a typical 3D data with size of 256×256×256, and most of the running time is spent by the OOF and GCs. It is obviously longer than the computation time of the methods in [14] and [29], both of which need less than 20 seconds for their core codes related to highly computational burden are run on the GPU. In the future, we will focus on increasing the robustness of the proposed method, and attempt to use the GPU-accelerated based algorithms to improve its efficiency.

5. Conclusions

This paper describes an effective liver-vessel segmentation and identification method based on oriented flux symmetry and GCs. It does not require any manual delineation of the object regions, and can also avoid complex training procedure like the machine learning method. The proposed method is initially inspired by two existing vessel detection measures including OOF and OFA. To cope with the intertwined and parallel liver vessels, we introduce these two measures to generate slenderized vessel image, and propose a novel vessel centerline extraction method by the combination of height ridge traversal and LNLG algorithm, which can not only automatically choose centerline seed points, but also show a good performance on the centerline extraction of thin vessels with low intensity as well as on the identification of different vessel centerlines. To effectively recognize liver vessels, an intensity model together with vessel boundary information captured by OFA measure is integrated into GCs for vessel segmentation, and a distance voting mechanism is designed to enable the identification of the different liver-vessel systems.

The developed approach is tested on six clinical CTA volumes. The experiment results indicate that our method is capable of dealing with various geometrical structures of liver vessels, and more thin vessels are contained compared with some existing vessel segmentation methods. In addition, as the OOF and OFA measures work effectively for the detection of general tubular structures, the proposed method can also be extended to the extraction of other 3D tubular structures.
.

References

[1] D. Selle, B. Preim, A. Schenk, H. O. Peitgen, Analysis of vasculature for liver surgical planning, IEEE Trans. Med. Imaging. 21 (11) (2002) 1344-1357, doi:10.1109/TMI.2002.801166.

[2] D. Lesage, E. D. Angelini, I. Bloch, G. Funka-Lea, A review of 3D vessel lumen segmentation techniques: models, features and extraction schemes, Med. Image Anal. 13 (6) (2009) 819-845, doi:10.1016/j.media.2009.07.011.

[3] A. F. Frangi, W. J. Niessen, K. L. Vincken, M. A. Viergever, Multiscale vessel enhancement filtering, MICCAI, 1998, pp. 130-137, doi:10.1007/BFb0056195.

[4] T. Jerman, F. Pernuš, B. Likar, Ž. Špiclin, Beyond Frangi: an improved multiscale vesselness filter, Proc. of SPIE, 2015, doi:10.1117/12.2081147.

[5] K. Krissian, G. Malandain, N. Ayache, R. Vaillant, Y. Trousset, Model-based detection of tubular structures in 3D images, Comput. Vis. Image Underst. 80 (2) (2000) 130-171, doi:10.1006/cviu.2000.0866.

[6] C. Y. Xiao, M. Staring, D. Shamonin, J. H. C. Reiber, J. Stolk, B. C. Stoel, A strain energy filter for 3D vessel enhancement with application to pulmonary CT images, Med. Image Anal. 15 (1) (2011) 112-124, doi:10.1016/j.media.2010.08.003.

[7] P. Yan, A. A. Kassim, Segmentation of volumetric MRA images by using capillary active contour, Med. Image Anal. 10 (3) (2006) 317-329, doi:10.1016/j.media.2005.12.002.

[8] M. W. K. Law, A. C. S. Chung, A deformable surface model for vascular segmentation, MICCAI, 2009, pp. 59-67, doi:10.1007/978-3-642-04271-3_8.

[9] Y. Cheng, X. Hu, J. Wang, Y. Wang, S. Tamura, Accurate vessel segmentation with constrained B-snake, IEEE Trans. Image Process. 24 (8) (2015) 2440-2455, doi:10.1109/TIP.2015.2417683.

[10] S. Esneault, C. Lafon, J. L. Dillenseger, Liver vessels segmentation using a hybrid geometrical moments/graph cuts method, IEEE Trans. Biomed. Eng. 57 (2) (2010) 276-283, doi:10.1109/TBME.2009.2032161.

[11] M. W. Law, A. C. S. Chung, Segmentation of intracranial vessels and aneurysms in phase contrast magnetic resonance angiography using multirange filters and local variances, IEEE Trans. Image Process. 22 (3) (2013) 845-859, doi:10.1109/TIP.2012.2216274.

[12] Y. Chi, J. Liu, S. K. Venkatesh, S. Huang, J. Zhou, Q. Tian, W. L. Nowinski, Segmentation of liver vasculature from contrast enhanced CT images using context-based voting, IEEE Trans. Biomed. Eng. 58 (8) (2011) 2144-2153, doi:10.1109/TBME.2010.2093523.

[13] M. Schneider, S. Hirsch, B. Weber, G. Szekely, B. H. Menze, Joint 3-D vessel segmentation and centerline extraction using oblique hough forests with steerable filters, Med. Image Anal. 19 (1) (2015) 220-249, doi:10.1016/j.media.2014.09.007.

[14] Y. Z. Zeng, Y. Q. Zhao, M. Liao, B. J. Zou, X. F. Wang, W. Wang, Liver vessel segmentation based on extreme learning machine, Phys. Medica. 32 (5) (2016) 709-716, doi:10.1016/j.ejmp.2016.04.003.

[15] H. Hemmati, A. Kamli-Asl, A. Talebpour, S. Shirani, Semi-automatic 3D segmentation of carotid lumen in contrast-enhanced computed tomography angiography images, Phys. Medica. 31 (8) (2015) 1098-1104, doi:10.1016/j.ejmp.2015.08.002.

[16] M. Liao, Y. Q. Zhao, X. Y. Liu, Y. Z. Zeng, B. J. Zou, X. F. Wang, F. Y. Shih, Automatic liver segmentation from abdominal CT volumes using graph cuts and border marching, Comput. Methods. Programs. Biomed. 143 (2017) 1–12, doi:10.1016/j.cmpb.2017.02.015.

[17] M. Liao, Y. Q. Zhao, W. Wang, Y. Z. Zeng, Q. Yang, F. Y. Shih, B. J. Zou, Efficient liver segmentation in CT images based on graph cuts and bottleneck detection, Phys. Medica. 32 (11) (2016) 1383-1396, doi:10.1016/j.ejmp.2016.10.002.

[18] P. Perona, J. Malik, Scale-space and edge detection using anisotropic diffusion, IEEE Trans. Pattern Anal. Mach. Intell. 12 (7) (1990) 629-639, doi:10.1109/34.56205.

[19] I. Bitter, R. V. Uitert, I. Wolf, L. Ibanez, J. M. Kuhnigk, Comparison of four freely available frameworks for image processing and visualization that use ITK, IEEE Trans. Vis. Comput. Graph. 13 (3) (2007) 483-493, doi:10.1109/TVCG.2007.1001.

[20] M. W. K. Law, A. C. S. Chung, Three dimensional curvilinear structure detection using optimally oriented flux, ECCV, 2008, pp. 368-382, doi:10.1007/978-3-540-88693-8_27.

[21] M. W. K. Law, A. C. S. Chung, An oriented flux symmetry based active contour model for three dimensional vessel segmentation, ECCV, 2010, pp. 720-734, doi:10.1007/978-3-642-15558-1_52.

[22] E. Türetken, C. Becker, P. Glowacki, F. Benmansour, P. Fua, Detecting irregular curvilinear structures in gray scale and color imagery using multi-directional oriented flux, ICCV, 2013, pp. 1553-1560, doi:10.1109/ICCV.2013.196.

[23] C. Bauer, T. Pock, E. Sorantin, H. Bischof, R. Beichel, Segmentation of interwoven 3d tubular tree structures utilizing shape priors and graph cuts, Med. Image Anal. 14 (2) (2010) 172-184, doi:10.1016/j.media.2009.11.003.

[24] J. A. Sethian. Level set methods and fast marching methods: Cambridge University Press; 1999.

[25] K. C. Ciesielski, P. A. V. Miranda, A. X. Falcao, J. K. Udupa, Joint graph cut and relative fuzzy connectedness image segmentation algorithm, Med. Image Anal. 17 (8) (2013) 1046-1057, doi:10.1016/j.media.2013.06.006.

[26] Q. Zheng, E. Q. Dong, Z. L. Cao, W. Y. Sun, Z. G. Li, Modified localized graph cuts based active contour model for local segmentation with surrounding nearby clutter and intensity inhomogeneity, Signal Process. 93 (4) (2013)

961-966, doi:10.1016/j.sigpro.2012.10.005.

[27] V. Caselles, R. Kimmel, G. Sapiro, Geodesic active contours, ICCV, 1995, pp. 694-699, doi:10.1109/ICCV.1995.466871.

[28] Y. Zhang, B. J. Matuszewski, L. K. Shark, C. J. Moore, Medical image segmentation using new hybrid level-set method, MEDIVIS '08. Fifth International Conference, 2008, pp. 71-76, doi:10.1109/MediVis.2008.12.

[29] E. Smistad, A. C. Elster, F. Lindseth, GPU accelerated segmentation and centerline extraction of tubular structures from medical images, Int. J. Comput. Assist. Radiol. Surg. 9 (4) (2014) 561-575, doi:10.1007/s11548-013-0956-x.

[30] C. Debbaut, P. Segers, P. Cornillie, C. Casteleyn, M. Dierick, W. Laleman, D. Monbaliu, Analyzing the human liver vascular architecture by combining vascular corrosion casting and micro-CT scanning: a feasibility study, J. Anat. 224 (4) (2014) 509-517, doi:10.1111/joa.12156.

[31] H. M. Luu, C. Klink, A. Moelker, W. Niessen, T. V. Walsum, Quantitative evaluation of noise reduction and vesselness filters for liver vessel segmentation on abdominal CTA images, Phys. Med. Biol. 60 (10) (2015) 3905-3926, doi:10.1088/0031-9155/60/10/3905.

[32] Y. Q. Zhao, X. H. Wang, X. F. Wang, F. Y. Shih, Retinal vessels segmentation based on level set and region growing, Pattern Recognit. 47 (7) (2014) 2437-2446, doi:10.1016/j.patcog.2014.01.006.